IEEE Access
Multidisciplinary | Rapid Review | Open Access Journal

Received July 28, 2019, accepted August 10, 2019, date of publication August 15, 2019, date of current version August 28, 2019.

Digital Object Identifier 10.1109/ACCESS.2019.2935472

Scattering Noise Model Enhanced EM-TV Algorithm for Benchtop X-ray Fluorescence Computed Tomography Image Reconstruction

SIYUAN ZHANG, LIANG LI, AND ZHIQIANG CHEN

Department of Engineering Physics, Tsinghua University, Beijing 100084, China
Key Laboratory of Particle and Radiation Imaging, Ministry of Education, Tsinghua University, Beijing 100084, China

Corresponding authors: Liang Li (lliang@tsinghua.edu.cn) and Zhiqiang Chen (czq@tsinghua.edu.cn)

This work was supported in part by the National Key R&D Program of China under Grant 2018YFC0115502, and in part by the National Natural Science Foundation of China (NSFC) under Grant 11775124 and Grant 11525521.

ABSTRACT Current benchtop x-ray fluorescence computed tomography (XFCT) devices, which use x-ray tubes to stimulate x-ray fluorescence (XRF) photons, suffer from the contamination of Compton scatter background produced by the polychromatic incident beam. The conventional maximum-likelihood expectation-maximization (ML-EM) algorithm only considers the noise model of the XRF signal, which results in high statistical noise in reconstructed images caused by scattered photons. In this study, we proposed a scattering noise model enhanced EM-TV algorithm for benchtop XFCT image reconstruction in order to reduce the noise of scatter background and improve the sensitivity of XFCT images. The statistical noise of scattered photons was considered in the likelihood function and the EM iteration step was modified correspondingly to suppress the statistical noise caused by Compton scattered photons. The robustness of the EM iteration was improved by applying the reweighted total variation (TV) norm as the penalty function. Numerical simulations and imaging experiments of a PMMA phantom consisting of gadolinium (Gd) solutions were performed to validate the proposed algorithm. The phantom was irradiated by a cone-beam polychromatic source and the projection was recorded by a linear-array photon counting detector. For comparison, the XFCT images of Gd were reconstructed using different algorithms. Results indicate that compared with the conventional ML-EM algorithm, the proposed algorithm can obtain XFCT images with lower background noise and higher contrast, which may further improve the sensitivity and image performance of current benchtop XFCT systems.

INDEX TERMS Image reconstruction, X-ray scattering, X-ray fluorescence computed tomography.

I. INTRODUCTION

X-ray fluorescence computed tomography (XFCT) is an element-specific imaging modality which has recently been proposed for imaging of High-Z elements (e.g. iodine (I), barium (Ba), gadolinium (Gd) and gold (Au)) in objects. As the projection data of XFCT is acquired by detecting the x-ray fluorescent (XRF) photons emitted from the target element, background tissues will not produce XRF signal, which results in high sensitivity and contrast of XFCT when detecting fluorescence materials [1], [2]. Therefore, XFCT has been considered as a promising approach to obtain the distribution of contrast probes (e.g. Gd/Au nanoparticles) in vivo [3], [4].

XFCT was first performed using synchrotron as the x-ray source [5], [6]. The synchrotron beam is monochromatic and linear polarized, which produces XRF signal with high intensity and low scatter background [7]. However, due to the limited access of synchrotron, recent studies focus more on the benchtop XFCT system using conventional x-ray tubes [8]–[10]. Two main shortcomings of current benchtop XFCT are the limited detection efficiency and the contamination of XRF signal with Compton scatter background. It is known that k-shell photoelectric cross section decreases with the increase of photon energy, which means a conventional polychromatic x-ray beam stimulates less XRF photons than a monochromatic beam with energy equal to the k-edge of the

The associate editor coordinating the review of this article and approving it for publication was Yi Zhang.

target element in same dose rate. In addition, the XRF projection data could be dominated by Compton scatter background with continuous spectrum. Although the expectation of scattered photons recorded by the detector can be well estimated, the statistical noise caused by scatter background is difficult to remove, which decreases the contrast and sensitivity of XFCT images.

In addition to the research efforts which are underway to decrease the scatter background utilizing the optimization of current benchtop XFCT devices [11]–[13], several studies are focused on image reconstruction algorithms [14]–[17] in order to reduce the impact of scattered photons and increase the image accuracy. Compared to other emission CT modalities (e.g. SPECT), the projection data of XFCT suffers more from the statistical noise caused by scattered photons. Traditional maximum-likelihood expectation-maximization (ML-EM) iterative algorithm [18] based only on noise model of the target signal is unable to suppress this kind of background noise effectively. Therefore, a ML approach with modeling of both XRF photons and scattered photons could be more appropriate for XFCT reconstruction [17].

In this work, we presented a scattering noise model enhanced EM-TV algorithm for XFCT image reconstruction in order to further reduce the statistical noise caused by Compton scatter background. The statistical noise of scattered photons was considered in the likelihood function and the system matrix was then expended correspondingly so that the XRF image and the scatter image could be updated in one iteration step. A reweighted total variation (TV) norm was applied as the penalty function to enhance the robustness of the EM iteration. Numerical simulations and phantom experiments were performed to investigate the reconstruction effect and accuracy of the proposed algorithm. Results show that compared to traditional ML-EM algorithm, the proposed method outperforms in robustness of iteration and suppression of the background noise caused by scattered photons, which significantly increases the contrast and sensitivity of current benchtop XFCT imaging.

II. MATERIALS AND METHODS

A. SYSTEM GEOMETRY

There are two main kinds of design for benchtop XFCT system. One is based on a single-pixel spectrometer with a pencil-beam source or a pencil-beam collimator [8], [9]. The other kind of design, which was discussed in this work (Fig. 1(b)), uses a cone-beam source to stimulate XRF photons and an array detector with pinhole collimation [19], [20]. As the two design have similar imaging physics, the algorithm presented in this work can be easily adjusted to the former by just modifying the system matrix.

As shown in Fig. 1(a), the acquisition of XRF signal consists of two steps. In the first step, the incident photons enter the object from an arbitrary point $\boldsymbol{A}$ and then stimulate XRF photons at point $\boldsymbol{B}$. In the second step, XRF photons

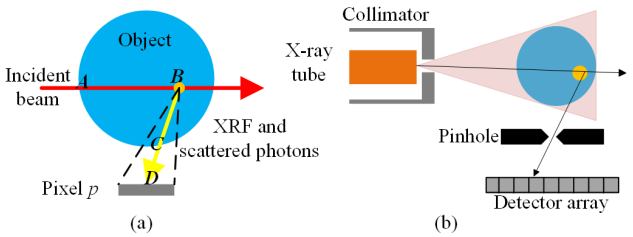

FIGURE 1. (a) Particle transport process of XFCT and (b) geometry of the benchtop XFCT system discussed in this work.

are recorded by the detector after exiting the object at point $\boldsymbol{C}$.

The number of XRF photons emitted from $\boldsymbol{B}$ and recorded by pixel p is

$$\begin{aligned} N^{(XRF)}{}_{B\to p} &= \int_{Aug} N^{(XRF)}{}_{B\to D} d\Omega \\ &= \int_{Aug}\int_0^{\infty} \left[I_0(E)\, e^{-\int_A^B \mu(E,l)dl}\, \omega\rho(B)\, \mu_{mpe} \right. \\ &\quad \left. \times (E,B)\, e^{-\int_B^{C_2} \mu(E_{xrf},l)dl} \right] dE d\Omega \end{aligned} \tag{1}$$

where Aug is the solid angle range covered by pixel p from point $\boldsymbol{B}$, I_0 is the intensity of the incident photons at energy E, μ is the linear attenuation coefficient along the path, μ_{mpe} is the photoelectric mass absorption coefficient of the fluorescence material, ω is the fluorescence yield and ρ is the concentration of fluorescence material.

Similar to XRF photons, the number of Compton scattered photons emitted from $\boldsymbol{B}$ and recorded by pixel p is

$$\begin{aligned} N^{(SC)}{}_{B\to p} &= \int_{Aug} N^{(SC)}{}_{B\to D} d\Omega \\ &= \int_{Aug}\int_0^{\infty} \left[I_0(E)\, e^{-\int_A^B \mu(E,l)dl}\, \mu_{co}(E,B) f_{KN} \right. \\ &\quad \left. \times (E, \theta_{SC}(\Omega))\, e^{-\int_B^{C_2} \mu(E_{sc},l)dl} \right] dE d\Omega \end{aligned} \tag{2}$$

where θ_{sc} is the scattering angle, μ_{co} is the Compton cross section and f_{KN} is the Klein–Nishina formula:

$$\begin{aligned} f_{KN}(E,\theta) &= \frac{d\sigma}{d\theta} \\ &= \pi r_0^2 sin\theta \frac{1+\cos^2\theta}{[1+\alpha(1-cos\theta)]^2} \\ &\quad \times \left(1 + \frac{\alpha^2(1-cos\theta)^2}{(1+\cos^2\theta)[1+\alpha(1-cos\theta)]} \right) \end{aligned} \tag{3}$$

where r_0 is the classical electron radius and $\alpha = E/(m_0c^2)$.

B. SCATTERING NOISE MODEL ENHANCED EM ALGORITHM

The goal of XFCT image reconstruction is to solve the following linear inverse problem:

$$P_i^{(XRF)} = \sum_{j=1}^{n} a_{ij}^{(XRF)} f_j \tag{4}$$

where $a^{(XRF)}$ denotes the system matrix of XRF photons which is determined by (1), f is the XFCT image to be reconstructed and $P^{(XRF)}$ is the XRF signal. As current benchtop XFCT devices use x-ray tubes to stimulate XRF photons, Compton scattered photons will also be produced by the polychromatic incident beam, which may contaminate the XRF signal. Therefore, the XRF signal needs to be extracted from the raw projection data before image reconstruction. The essence of the ''scatter correction'' method is to estimate the expectation of scattered photons recorded by the target energy bin. Then $P^{(XRF)}$ can be calculated as

$$P_i^{(XRF)} = P_i^{(T)} - P_i^{(S)} \tag{5}$$

where $P^{(T)}$ is the raw projection data collected by the target energy bin and$P^{(S)}$ is the estimation of scattered photons in the target bin. In practical applications, $P^{(S)}$ was always estimated using fitted spectrum [8] or nearby energy bins [21].

As the number of XRF photons emitted from each image pixel has Poisson probability distribution, the well-known ML-EM iteration algorithm was applied to solve the problem in most studies. We assume that x_{ij} is the count of XRF photons emitted from image pixel j and recorded by detector pixel i, then the likelihood function is

$$L(f, x) = \prod_{i=1}^{m} \prod_{j=1}^{n} \frac{\mathrm{e}^{-a_{ij}^{(XRF)} f_j} \left(x_{ij}\right)^{a_{ij}^{(XRF)} f_j}}{\left(x_{ij}\right)!} \tag{6}$$

Therefore, the iteration step of ML-EM algorithm [18] can be expressed as

$$f_j^{(k+1)} = \frac{f_j^{(k)}}{\sum_{i=1}^{m} a_{ij}^{(XRF)}} \sum_{i=1}^{m} \frac{P_i^{(XRF)}}{\sum_{j'=1}^{n} a_{ij'}^{(XRF)} f_{j'}^{(k)}} a_{ij}^{(XRF)} \tag{7}$$

However, the statistical noise caused by scattered photons is ignored in (6), which may result in more background noise. According to (2), the particle transport process of Compton scattered photons is similar to XRF photons, which means that the scattered photons can be considered as another kind of ''signal''. Therefore, we proposed an enhanced EM iteration algorithm based on both XRF and scattered photons in this work in order to reduce the statistical noise caused by Compton scatter background.

For the projection data with scatter background, (4) should be modified to

$$\begin{cases} P_i^{(T)} = \sum_{j=1}^{n} a_{ij}^{(XRF)} f_j + \sum_{j=1}^{n} a_{ij}^{(SCA)} s_j \\ P_i^{(S)} = \sum_{j=1}^{n} a_{ij}^{(SCA)} s_j \end{cases} \tag{8}$$

where $a^{(SCA)}$ denotes the system matrix of scattered photons which is determined by (2), s is the distribution of scatter background to be reconstructed.

We assume that

$$\begin{cases} P^{(ALL)} = \left(P_1^{(T)}, P_2^{(T)}, \cdots, P_n^{(T)}, P_1^{(S)}, P_2^{(S)}, \cdots, P_n^{(S)}\right)^{\mathrm{T}} \\ f^{(ALL)} = (f_1, f_2, \cdots, f_m, s_1, s_2, \cdots, s_m)^{\mathrm{T}} \\ a^{(ALL)} = \begin{bmatrix} a^{(XRF)} & a^{(SCA)} \\ 0 & a^{(SCA)} \end{bmatrix} \end{cases} \tag{9}$$

Then (8) can be rewritten as

$$P_i^{(ALL)} = \sum_{j=1}^{2n} a_{ij}^{(ALL)} f_j^{(ALL)} \tag{10}$$

Therefore, the EM step of $f^{(ALL)}$ is

$$f_j^{(ALL)(k+1)} = \frac{f_j^{(ALL)(k)}}{\sum_{i=1}^{2m} a_{ij}^{(ALL)}} \sum_{i=1}^{2m} \frac{P_i^{(ALL)}}{\sum_{j'=1}^{2n} a_{ij'}^{(ALL)} f_{j'}^{(ALL)(k)}} a_{ij}^{(ALL)} \tag{11}$$

For XFCT image, the scattering noise model enhanced EM iteration can be expressed as

$$\begin{aligned} f_j^{(k+1)} &= f_j^{(ALL)(k+1)}_{1 \le j \le n} \\ &= \frac{f_j^{(k)}}{\sum_{i=1}^{m} a_{ij}^{(XRF)}} \\ &\quad \times \sum_{i=1}^{m} \frac{P_i^{(T)}}{\sum_{j'=1}^{n} \left(a_{ij'}^{(XRF)} f_{j'}^{(k)} + a_{ij'}^{(SCA)} s_{j'}^{(k)}\right)} a_{ij}^{(XRF)} \end{aligned} \tag{12}$$

C. REWEIGHTED TV NORM

Unfortunately, the performance of conventional ML-EM algorithm in its practical application deteriorates when the iteration number gets larger so that the iteration has to be stopped before the ''checkerboard effect'' shows up [22]. Previous studies indicated that this problem can be overcome by including a priori information [23]. In order to improve the robustness of the iteration algorithm, a developed one-step-late (OSL) method [24] was applied which modifies (12) as

$$\begin{aligned} f_j^{(k+1)} &= \left(1 - \beta U_j^{(k)}\right) \frac{f_j^{(k)}}{\sum_{i=1}^{m} a_{ij}^{(XRF)}} \\ &\quad \times \sum_{i=1}^{m} \frac{P_i^{(T)}}{\sum_{j'=1}^{n} \left(a_{ij'}^{(XRF)} f_{j'}^{(k)} + a_{ij'}^{(SCA)} s_{j'}^{(k)}\right)} a_{ij}^{(XRF)} \end{aligned} \tag{13}$$

where U is the derivative of a penalty function V and β is the control parameter. In this work, a reweighted TV norm [25] was applied as the penalty function which can be

expressed as

$$U_{i,j}^{(k)} = \frac{\partial\left(\sum_{i,j}\sqrt{\left(f_{i,j}-f_{i,j+1}\right)^2+\left(f_{i,j}-f_{i,+1j}\right)^2}\right)/\partial f_{i,j}^{(k)}}{\sqrt{\left(f_{i,j}^{(k)}-f_{i,j+1}^{(k)}\right)^2+\left(f_{i,j}^{(k)}-f_{i+1,j}^{(k)}\right)^2+\varepsilon}} \tag{14}$$

where ε is a small value preventing the denominator to be zero.

Finally, the scattering noise model enhanced EM-TV iteration algorithm proposed in this work can be expressed as

$$\begin{cases} f_j^{(k+1)} = \dfrac{\left(1-\beta U_j^{(k)}\right)f_j^{(k)}}{\sum_{i=1}^m a_{ij}^{(XRF)}{}_{ij}} \times \sum_{i=1}^m \dfrac{P_i^{(T)}}{\sum_{j'=1}^n \left(a_{ij'}^{(XRF)} f_{j'}^{(k)} + a_{ij'}^{(SCA)} s_{j'}^{(k)}\right)} a_{ij}^{(XRF)} \\ s_j^{(k+1)} = \dfrac{s_j^{(k)}}{\sum_{i=1}^m a_{ij}^{(SCA)}{}_{ij}} \times \sum_{i=1}^m \dfrac{P_i^{(S)}}{\sum_{j'=1}^n a_{ij'}^{(SCA)} s_{j'}^{(k)}} a_{ij}^{(SCA)} \end{cases} \tag{15}$$

III. RESULTS

A set of numerical simulations and experiments performed under similar conditions were demonstrated in this section. As shown in Fig. 1(b), the benchtop XFCT device in this work consists of a conventional x-ray tube to produce incident x-rays and a linear array photon counting detector with pinhole collimation to record XRF signal. Gd (k$\alpha \approx$ 42.5 keV) was used as the fluorescence material and the threshold was set at 35, 40, 45 and 50 keV. As the proportion of scattered photons record by each energy bin depends on (2) and (3), the expectation of scattered photons in the target bin (40-45 keV) was estimated by the count in the nearby bins (35-40 keV and 45-50 keV) [20]. The materials of the objects in this work were assumed to be known and the attenuation coefficients were obtained from National Institute of Standards and Technology (NIST). All the MATLAB programs about reconstruction algorithms ran on a desktop computer with Intel(R) Core(TM) i9-7940X CPU @ 3.10 GHz and 128 GB RAM. The time cost per iteration was about 0.08 s for ML-EM, 0.17 s for enhanced EM and 0.17 s for enhanced EM-TV.

A. NUMERICAL SIMULATION

Numerical simulations were performed to evaluate the accuracy and robustness of the proposed reconstruction algorithm. The phantom used in the simulations was a PMMA cylinder with Gd insertions (Fig. 2(a)). The spectrum of the incident beam (150 kVp filtered by 0.5 mm copper (Cu)) was simulated by SpekCalc (Fig. 2(b)) [26]. The XRF signal was assumed to be acquired by a linear array detector with

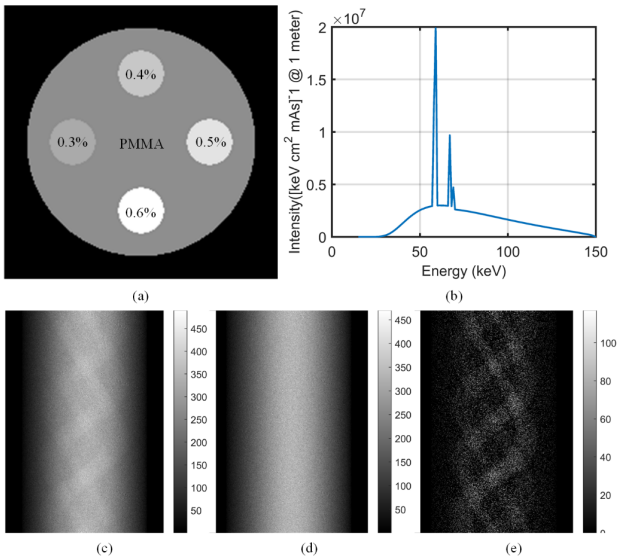

FIGURE 2. (a) PMMA phantom inserted with Gd solutions; (b) spectrum of the incident beam used in simulations. (c) raw projection recorded by the target bin (40-45 keV); (d) estimation of scattered photons in raw projection and (e) XRF signal extracted from raw projection by subtracting the estimation of scatter background.

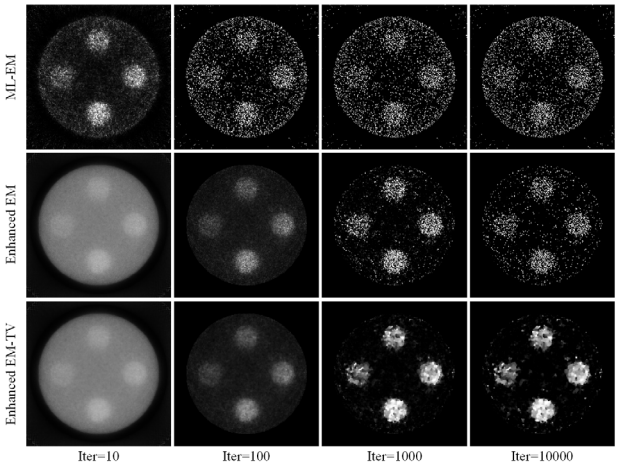

FIGURE 3. XFCT images reconstructed by different iteration algorithms. The grayscale of each image is [0 0.7%].

256 pixels and 360 projections were obtained with the dose of 10 mAs per projection.

For comparison, three iteration algorithms were used to reconstruct the XFCT image: the conventional ML-EM algorithm, the enhanced EM algorithm and the enhanced EM-TV algorithm ($\beta = 0.01$). The reconstructed XFCT images with different number of iterations are shown in Fig. 3. The root mean squared error (RMSE) and contrast to noise ratio (CNR) of each image are shown in Fig. 4. According to the results, the conventional ML-EM algorithm tends to converge faster, which is probably because the XRF signal has already been extracted from the raw projection data before image reconstruction (Fig. 2(e)). On the other hand, the statistical noise caused by scattered photons has not been considered or suppressed during the iteration, which resulted in more

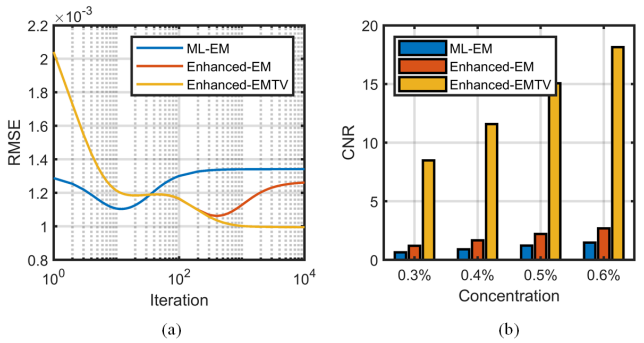

FIGURE 4. (a) RMSE of the reconstructed XFCT images using different iteration algorithms and (b) CNR of XFCT images with the iteration number of 10000.

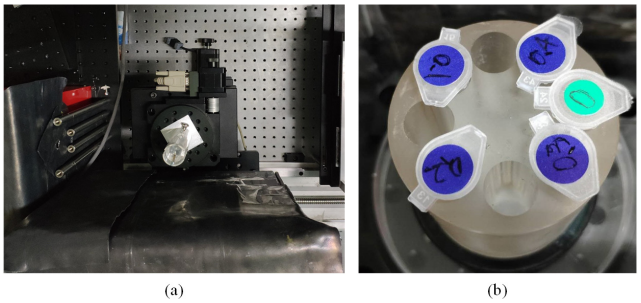

FIGURE 5. (a) The experimental XFCT device and (b) the PMMA phantom used in the experiments.

background noise. It can be seen that the noise caused by scattered photons has been effectively reduced by the enhanced EM algorithm. However, the image still got noisier with the increasing of iteration number. This kind of noise caused by the ill-posed inverse problem could be suppressed by penalty function (reweighted TV norm in this work) so that the enhanced EM-TV obtained the reconstructed image with the lowest noise level and the highest accuracy.

B. PHANTOM EXPERIMENT

The phantom experiments were performed using our experimental XFCT system (Fig. 5(a)) [21]. The phantom used in the experiments (Fig. 5(b)) was a PMMA cylinder which is 5 cm in diameter. The phantom was inserted with water and $Gd(NO_3)_3$ solutions (0.1%, 0.2%, 0.3% and 0.4%). The incident beam was produced by a micro-focus x-ray tube (150 kV, 0.5 mA, L12161-07, Hamamatsu) and was filtered with 0.4 mm Cu. The projection data was acquired by a CdZnTe detector (eV-3500) which has 256 pixels with the size of each pixel being 0.5 mm × 2 mm. The tungsten collimator with a rectangular pinhole (0.5 × 2 mm) was placed between the rotation stage and the detector. 360 projections were acquired with the scan time of 10 s per projection.

The XFCT images reconstructed by different algorithms are shown in Fig. 6. The CNR of Gd in each reconstructed image was calculated and listed in Table 1. It can be seen that the comparison of reconstructed results was in agreement with numerical simulations. When using conventional ML-EM algorithm, the regions of Gd insertions were

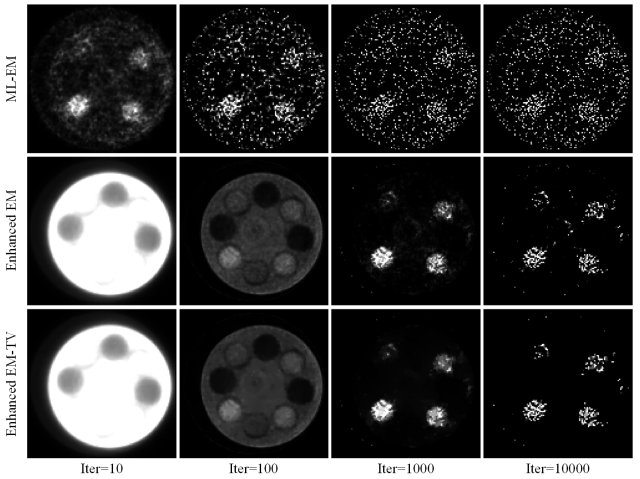

FIGURE 6. XFCT images reconstructed by different iteration algorithms. The grayscale of each image is [0 0.6%].

TABLE 1. CNR of Gd solutions using different reconstruction algorithms.

Algorithm	CNR			
	0.1%	0.2%	0.3%	0.4%
ML-EM	0.55	1.09	1.58	2.32
Enhanced EM	18.84	50.50	82.70	126.81
Enhanced EM-TV	48.93	140.22	227.75	346.93

dominated by the statistical noise of the scattered photons emitted from the whole PMMA phantom. The enhanced EM algorithm effectively reduced the scatter noise so that each Gd insertion was clearly visible in the reconstructed image. The noise caused by the increasing iteration number was further suppressed by reweighted TV norm and the distribution of Gd solutions with low concentrations was more reliable in the XFCT image reconstructed by the enhanced EM-TV algorithm.

IV. DISCUSSION

As the number of scattered photons in XFCT projection depends on the incident beam and the size of the whole object, the XRF signal will be severely interfered by scattered photons especially at low concentrations of fluorescence probes. Therefore, compared to the fluctuation of XRF photons, the statistical noise of scatter background has greater impact on XFCT images in most cases. The results demonstrated in this work indicate that the enhanced EM algorithm can effectively improve the sensitivity of benchtop XFCT system by reducing the background noise caused by the scattered photons.

A reweighted TV norm was applied as the penalty function of the proposed iteration algorithm. According to Zeng's study [24], (13) can be rewritten as

$$f_j^{(k+1)} = f_j^{(k)} - \lambda_1 U_j^{(k)} - \lambda_2 \sum_{i=1}^{m} a_{ij}^{(XRF)} w_i \times \left[\sum_{j'=1}^{n} a_{ij'}^{(XRF)} f_{j'}^{(k)} - \left(P_i^{(T)} - \sum_{j'=1}^{n} a_{ij'}^{(SCA)} s_{j'}^{(k)} \right) \right] \quad (16)$$

where

$$\begin{cases} \lambda_1 = \dfrac{\beta f_j^{(k)}}{\sum_{i=1}^{m} a_{ij}^{(XRF)}} \sum_{i=1}^{m} \dfrac{P_i^{(T)} a_{ij}^{(XRF)}}{\sum_{j'=1}^{n} a_{ij'}^{(XRF)} f_{j'}^{(k)} + \sum_{j'=1}^{n} a_{ij'}^{(SCA)} s_{j'}^{(k)}} \\ \lambda_2 = \dfrac{f_j^{(k)}}{\sum_{i=1}^{m} a_{ij}^{(XRF)}} \\ w_i = \dfrac{1}{\sum_{j'=1}^{n} a_{ij'}^{(XRF)} f_{j'}^{(k)} + \sum_{j'=1}^{n} a_{ij'}^{(SCA)} s_{j'}^{(k)}} \end{cases} \tag{17}$$

Then (13) intends to minimize the following objective function:

$$F = V + \frac{1}{2} \left\| W \left[A^{(XRF)} F - \left(P^{(T)} - S \right) \right] \right\|^2 \tag{18}$$

Therefore, the reweighted TV norm in this work can be considered as the regularization item. It is notice that this ''reweighted norm'' was usually used as a proxy for the L0 minimization [27]. But in this work, the function of the reweighted TV norm was to enhance the robustness of EM iteration. As shown in Fig. 4(a), the error of the images reconstructed by conventional EM iteration became larger with the increase of the iteration number due to the ''checkerboard'' effect, while the image reconstructed by EM-TV iteration had the lowest RMSE, which indicates that the accuracy and robustness of the proposed algorithm was effectively enhanced by the reweighted TV norm.

Compared to the ML-EM algorithm, the system matrix of scattered photons $a^{(SCA)}$ was a new parameter added to the enhanced EM and the ''scatter image'' was reconstructed and updated synchronously during the iteration. As the spectrum and cross section of Compton scattered photons are much more complex than XRF photons, the calculation of $a^{(SCA)}$ may not be much accurate. However, the error of the ''scatter image'' only influences the scatter noise model and has no impact on the accuracy of the XFCT image. According to (8), the accuracy of the XFCT image still depends on the estimation of the ''scatter projection'' $P^{(S)}$ so that the theoretical error of the enhanced EM algorithm will not increase by adding the new parameter $a^{(SCA)}$.

One of the main shortcomings of the proposed algorithm is that the convergence rate of the enhanced EM iteration is relatively slower than conventional algorithms. For ML-EM algorithm, the expectation of scattered photons was already removed in the projection data. On the other hand, the distribution of scatter background had to be calculated and updated during the iteration when using the enhanced EM algorithm, which may lead to a slower convergence rate. Further approach to the acceleration of the current iteration strategy will be investigated and discussed in our future research.

V. CONCLUSION

A scattering noise model enhanced EM-TV algorithm was presented in this work. The performance of the proposed algorithm was validated by numerical simulations and phantom experiments. As the scatter noise model was considered in the likelihood function, the statistical noise caused by Compton scattered photons was effectively suppressed. The robustness of the EM iteration was improved by applying the reweighted TV norm as the penalty function. Compared with conventional ML-EM algorithm, the proposed algorithm can obtain XFCT images with lower background noise and higher contrast, which may further improve the sensitivity and image performance of current benchtop XFCT systems.

REFERENCES

[1] M. Bazalova, Y. Kuang, G. Pratx, and L. Xing, ''Investigation of X-ray fluorescence computed tomography (XFCT) and K-edge imaging,'' *IEEE Trans. Med. Imag.*, vol. 31, no. 8, pp. 1620–1627, Aug. 2012.
[2] P. Feng, W. Cong, B. Wei, and G. Wang, ''Analytic comparison between X-ray fluorescence CT and K-edge CT,'' *IEEE Trans. Biomed. Eng.*, vol. 61, no. 3, pp. 975–985, Mar. 2014.
[3] N. Manohar, F. J. Reynoso, P. Diagaradjane, S. Krishnan, and S. H. Cho, ''Quantitative imaging of gold nanoparticle distribution in a tumor-bearing mouse using benchtop X-ray fluorescence computed tomography,'' *Sci. Rep.*, vol. 6, Feb. 2016, Art. no. 022079.
[4] S. Zhang, L. Li, J. Chen, Z. Chen, W. Zhang, and H. Lu, ''Quantitative imaging of Gd nanoparticles in mice using benchtop cone-beam X-ray fluorescence computed tomography system,'' *Int. J. Mol. Sci.*, vol. 20, no. 9, p. 2315, May 2019.
[5] P. Boisseau and L. Grodzins, ''Fluorescence tomography using synchrotron radiation at the NSLS,'' *Hyperfine Interact.*, vol. 33, nos. 1–4, pp. 283–292, Mar. 1987.
[6] G. Fu, L.-J. Meng, P. Eng, M. Newville, P. Vargas, and P. La Riviere, ''Experimental demonstration of novel imaging geometries for X-ray fluorescence computed tomography,'' *Med. Phys.*, vol. 40, no. 6, Jun. 2013, Art. no. 061903.
[7] T. Takeda, Q. Yu, T. Yashiro, T. Yuasa, Y. Hasegawa, Y. Itai, and T. Akatsuka, ''Human thyroid specimen imaging by fluorescent X-ray computed tomography with synchrotron radiation,'' *Proc. SPIE*, vol. 3772, Sep. 1999, Art. no. 363728.
[8] S. K. Cheong, B. L. Jones, A. K. Siddiqi, F. Liu, N. Manohar, and S. H. Cho, ''X-ray fluorescence computed tomography (XFCT) imaging of gold nanoparticle-loaded objects using 110 kVp X-rays,'' *Phys. Med. Biol.*, vol. 55, no. 3, pp. 647–662, Feb. 2010.
[9] Y. Kuang, G. Pratx, M. Bazalova, B. Meng, J. Qian, and L. Xing, ''First demonstration of multiplexed X-ray fluorescence computed tomography (XFCT) imaging,'' *IEEE Trans. Med. Imag.*, vol. 32, no. 2, pp. 262–267, Feb. 2013.
[10] M. F. Ahmed, S. Yasar, and S. H. Cho, ''A Monte Carlo model of a benchtop X-ray fluorescence computed tomography system and its application to validate a deconvolution-based X-ray fluorescence signal extraction method,'' *IEEE Trans. Med. Imag.*, vol. 37, no. 11, pp. 2483–2492, Nov. 2018.
[11] M. Ahmad, M. Bazalova, L. Xiang, and L. Xing, ''Order of magnitude sensitivity increase in X-ray fluorescence computed tomography (XFCT) imaging with an optimized spectro-spatial detector configuration: Theory and simulation,'' *IEEE Trans. Med. Imag.*, vol. 33, no. 5, pp. 1119–1128, May 2014.
[12] N. Manohar, B. L. Jones, and S. H. Cho, ''Improving X-ray fluorescence signal for benchtop polychromatic cone-beam X-ray fluorescence computed tomography by incident X-ray spectrum optimization: A Monte Carlo study,'' *Med. Phys.*, vol. 41, no. 10, Oct. 2014, Art. no. 101906.
[13] D. Vernekohl, S. Tzoumas, W. Zhao, and L. Xing, ''Polarized X-ray excitation for scatter reduction in X-ray fluorescence computed tomography,'' *Med. Phys.*, vol. 45, no. 8, pp. 3741–3748, Aug. 2018.
[14] P. La Riviere, ''Accurate analytic reconstruction in X-ray fluorescence computed tomography,'' in *Proc. IEEE Int. Symp. Biomed. Imag.*, Jul. 2002, pp. 637–640.

[15] P. J. La Rivière, D. M. Billmire, P. Vargas, M. L. Rivers, and S. R. Sutton, "Penalized-likelihood image reconstruction for X-ray fluorescence computed tomography," *Opt. Eng.*, vol. 45, no. 7, Jul. 2006, Art. no. 077005.
[16] M. F. Ahmed, S. Yasar, and S. H. Cho, "Development of an attenuation correction method for direct X-ray fluorescence (XRF) imaging utilizing gold L-shell XRF photons," *Med. Phys.*, vol. 45, no. 12, pp. 5543–5554, Dec. 2018.
[17] T. Sasaya, N. Sunaguchi, T. Thet-Lwin, K. Hyodo, T. Zeniya, T. Takeda, and T. Yuasa, "Dual-energy fluorescent X-ray computed tomography system with a pinhole design: Use of K-edge discontinuity for scatter correction," *Sci. Rep.*, vol. 7, Mar. 2017, Art. no. 044143.
[18] K. Lange and R. Carson, "EM reconstruction algorithms for emission and transmission tomography," *J. Comput. Assist. Tomogr.*, vol. 8, no. 2, pp. 306–316, Apr. 1984.
[19] T. Sasaya, N. Sunaguchi, K. Hyodo, T. Zeniya, and T. Yuasa, "Multi-pinhole fluorescent X-ray computed tomography for molecular imaging," *Sci. Rep.*, vol. 7, p. 5742, Jul. 2017.
[20] S. Zhang, L. Li, R. Li, and Z. Chen, "Full-field fan-beam X-ray fluorescence computed tomography system design with linear-array detectors and pinhole collimation: A rapid Monte Carlo study," *Opt. Eng.*, vol. 56, no. 11, Nov. 2017, Art. no. 113107.
[21] L. Li, S. Zhang, R. Li, and Z. Chen, "Full-field fan-beam X-ray fluorescence computed tomography with a conventional X-ray tube and photon-counting detectors for fast nanoparticle bioimaging," *Opt. Eng.*, vol. 56, no. 4, Apr. 2017, Art. no. 043106.
[22] G. T. Herman and D. Odhner, "Performance evaluation of an iterative image reconstruction algorithm for positron emission tomography," *IEEE Trans. Med. Imag.*, vol. 10, no. 3, pp. 336–346, Sep. 1991.
[23] P. J. Green, "Bayesian reconstructions from emission tomography data using a modified EM algorithm," *IEEE Trans. Med. Imag.*, vol. 9, no. 1, pp. 84–93, Mar. 1990.
[24] L. Zeng, "Extension of emission EM look-alike algorithms to Bayesian algorithms," *Proc. SPIE*, vol. 11072, May 2019, Art. no. 110720N.
[25] M. Chang, L. Li, Z. Q. Chen, Y. S. Xiao, L. Zhang, and G. Wang, "A few-view reweighted sparsity hunting (FRESH) method for CT image reconstruction," *J. X-Ray Sci. Technol.*, vol. 21, no. 2, pp. 161–176, 2013.
[26] G. Poludniowski, G. Landry, F. DeBlois, P. M. Evans, and F. Verhaegen, "SpekCalc: A program to calculate photon spectra from tungsten anode X-ray tubes," *Phys. Med. Biol.*, vol. 54, no. 19, p. N433, Oct. 2009.
[27] E. J. Candès, M. B. Wakin, and S. P. Boyd, "Enhancing sparsity by reweighted ℓ_1 minimization," *J. Fourier Anal. Appl.*, vol. 14, nos. 5–6, pp. 877–905, Dec. 2008.

SIYUAN ZHANG received the B.S. degree from Tsinghua University, China, in 2015, where he is currently pursuing the Ph.D. degree. His current research interests include X-ray fluorescence CT system design and image reconstruction.

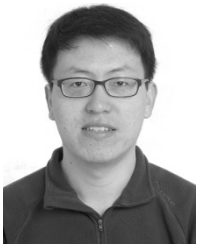

LIANG LI received the B.S. and Ph.D. degrees from Tsinghua University, Beijing, China, in 2002 and 2007, respectively, where he is currently an Associate Professor with the Department of Engineering Physics. He has authored 140 peer-reviewed journal and conference papers. His research interests include mathematical and physical problems of X-ray imaging and its medical, industrial, and other applications, especially the reconstruction problems under the special imaging conditions.

ZHIQIANG CHEN received the Ph.D. degree in engineering physics from Tsinghua University, Beijing, China, in 1999, where he is currently a Professor with the Department of Engineering Physics. His research interests include X-ray imaging, computed tomography, image processing, and reconstruction.